Check for
updates

Experimental and Numerical Study of Composite Honeycomb Sandwich Structures Under Low-Velocity Impact

Yunfei Deng[1] · Xiaoyu Hu[1] · Yijie Niu[1] · Yimei Zheng[1] · Gang Wei[1]

Abstract

The experimental and numerical investigations on the dynamic responses and failure mechanisms of honeycomb panels under low-velocity impact were carried out in the present work. The carbon fiber composite hexagonal honeycomb panels were fabricated using the hot press molding method. Then, low-velocity drop-weight impact tests on the composite honeycomb panels were conducted under impact energy levels of 5J, 10J, 30J, 50J, 60J, 70J, and 100J to study the deformation mechanisms and damage modes. The VUMAT was developed to model the behavior of sandwich panels, in which a progressive damage model based on the strain-based failure criterion of composite fabric and Yeh delamination failure criteria was implemented in ABAQUS/Explicit. Two-dimensional topological honeycomb configurations with the same relative density were established. The energy absorption and load-bearing capacity of hexagonal, square, triangular, Kagome, and two kinds of circular (CS and CH types) honeycombs under 100J impact energy were discussed. The results showed that the circular honeycomb (CH type) had the largest first peak force of 6.714 kN, while the hexagonal honeycomb had the smallest first peak force of 3.715 kN. Compared with hexagonal honeycomb, the energy absorption of the triangle, Kagome, and circular honeycombs (CH type) were increased by 37.15%, 38.18%, and 47.06%, respectively. This study provided a series of experimental and numerical results, which could provide a reference for selecting suitable honeycomb configurations in the protection field.

Keywords Carbon fiber composite honeycomb · Low-velocity impact · Deformation process · Damage modes · Finite element analysis

1 Introduction

Honeycomb, as a major lightweight structure, is widely used in the aerospace and transportation field due to its excellent mechanical properties and versatility [1]. In recent years, the combination of composite materials and sandwich structures has opened up new ideas for

✉ Xiaoyu Hu
    2021012112@cauc.edu.cn

✉ Yimei Zheng
    3122134855@qq.com

[1] College of Aeronautical Engineer, Civil Aviation University of China, Tianjin 300300, China

lightweight design and multifunctional application [2–4]. All-composite sandwich structures have become a research hotspot [5, 6]. However, composite is often quite sensitive to environment and impact damage [7–9]. In practice, it is vulnerable to various impacts such as objects falling and collisions [10]. Under the action of lower impact energy, evident internal damage will occur, resulting in a significant reduction in structural strength and stiffness [11, 12]. Therefore, an in-depth understanding of low-velocity impact behavior and failure mechanisms will be necessary for more reliable applications [13].

A series of studies on composite honeycomb panels have been carried out. Wei et al. [5] summarized the preparation technology of composite honeycomb sandwich structures. Besides, a preliminary study on the static mechanical properties was carried out, such as compression [14], bending [15], etc. However, the dynamic mechanical properties of composite honeycomb panels were still insufficient. Li et al. [16] studied the influence of the impactor nose shape on dynamic responses and failure mechanisms of carbon fiber reinforced plastic (CFRP) Kagome lattice core sandwich panels subjected to low-velocity impact. Zeng et al. [17] experimentally and numerically investigated the dynamic responses of composite sandwich structures with reentrant honeycomb cores subjected to impulsive loading. Yu et al. [18] conducted a series of ballistic impact tests on composite sandwich structures with Y-shaped cores. The results showed that the impact resistance of sandwich panels was better than that of laminates.

The most prominent feature of the honeycomb sandwich structure is the extreme designability of the cell geometry. Even though the cells have similar overall dimensions and densities, the geometry of each cell can be very different. It results in unique mechanical and other properties that reflect the unlimited potential of honeycomb sandwich structures [19]. Due to the wide range of unit geometries, complex mechanical properties, and multifunctional requirements can be accommodated by designing configurations and geometrical parameters.

In many engineering applications, the impact resistance of sandwich structures is still an important research topic. Changing the dimensional parameters or materials is a common method to improve the strength of sandwich structures. Sun et al. systematically studied the effects of structural parameters (such as skin thickness, core height, cell wall thickness, and cell size) of hexagonal honeycomb panels on the static [20, 21] and dynamic [22, 23] mechanical properties. The results showed that reasonable adjustment of cell geometric parameters can effectively improve the mechanical properties of honeycomb sandwich structures.

The unit cell configuration has a notable effect on the overall mechanical properties [24]. The design of core configuration is also a meaningful way to improve the strength of honeycomb panels [25]. Pehlivan and Baykasoğlu [26] carried out quasi-static compression experiments on carbon fiber reinforced polymer (CFRP) honeycombs with different core configurations. The hexagonal honeycomb specimens generally showed superior compressive performance compared to the square and circular specimens. In the out-of-plane compression experiment, it was found that the average dynamic stress of the typical collapse strength of the membrane-dominated honeycomb (such as square, triangular, and Kagome structures) was higher than that of the bending-dominated honeycomb (such as hexagonal and rhombic structures) [27].

Due to the diversity of cell substrates and filling materials, as well as the difference in cell arrangement methods at all levels, the deformation mechanisms and energy absorption of various filled multi-cell impact protection structures under different velocities and boundary conditions are different. Therefore, their dynamic responses characteristics may also differ in significant way [28]. In the experimental study of ballistic penetration, Wang

et al. [29] found that the anti-out-of-plane penetration ability of circular honeycomb was better than that of triangular, square, hexagonal, and negative Poisson's ratio honeycombs. At the same time, in the study of blast resistance, it was found that the energy absorption of AuxHex and Star-Reentrant honeycomb was better than that of other configurations [30].

In summary, research on the mechanisms of geometrical parameters on the mechanical behavior of honeycombs has been extensive. However, the mechanical properties of honeycomb sandwich panels with different cell configurations under different impact loading conditions are different. Especially, the crushing mechanisms of the composite honeycomb panels under low-velocity impact is still unclear. This paper intends to investigate the low-velocity impact responses of carbon fiber composite honeycombs (CFCHs) with different core configurations. Firstly, hexagonal honeycomb panels were prepared and subjected to low-velocity impact experiments. The dynamic responses process was comprehensively analyzed from force, displacement, and energy absorption. Besides, the damage modes were obtained by microscope. A three-dimensional progressive damage model for composite materials was also developed to assess the damage mechanisms of composite honeycomb panels. The influence of unit cell configurations on low-velocity impact performance was clarified, providing reliable design guidance for the design of honeycomb panels.

2 Fabrication and Experiments

2.1 Preparation Process of Composite Honeycomb Panels

The hexagonal honeycomb core and face sheets were prepared from plain woven carbon fiber prepreg (CYCOM® 97714A/PWC T300 3K ST) produced by Solvay Co., Ltd., and the thickness of single layer prepreg was 0.25 mm. The material properties of the prepreg are shown in Table 1. The fiber areal weight was 193 g/m^2. The stacking sequences of face sheets and core were [0°/90°]$_s$ and [0°/90°], respectively. As illustrated in Fig. 1(b), each hexagonal cell had a cell size L of 6 mm and a core height H_c of 20 mm. The thickness of the face sheet H_f and cell wall t were 1mm and 0.5mm, respectively. The relative density of the composite honeycomb panels (120 mm×120 mm×22 mm) is 12.83%, which is similar to the S-type foldcore [31], as shown in Fig. 1(c).

The preparation process of the CFCHs was divided into two main parts. The face sheets were cured using the vacuum bag molding process. The prepreg was covered with release film, metal board, electric heating blanket, insulation cotton, and vacuum bag, as shown in Fig. 2(a). During the preparation process, the vacuum pump was opened to keep the pressure constant at atmospheric pressure. At the same time, the thermal

Table 1 Material properties of the carbon fiber/epoxy prepreg [32]

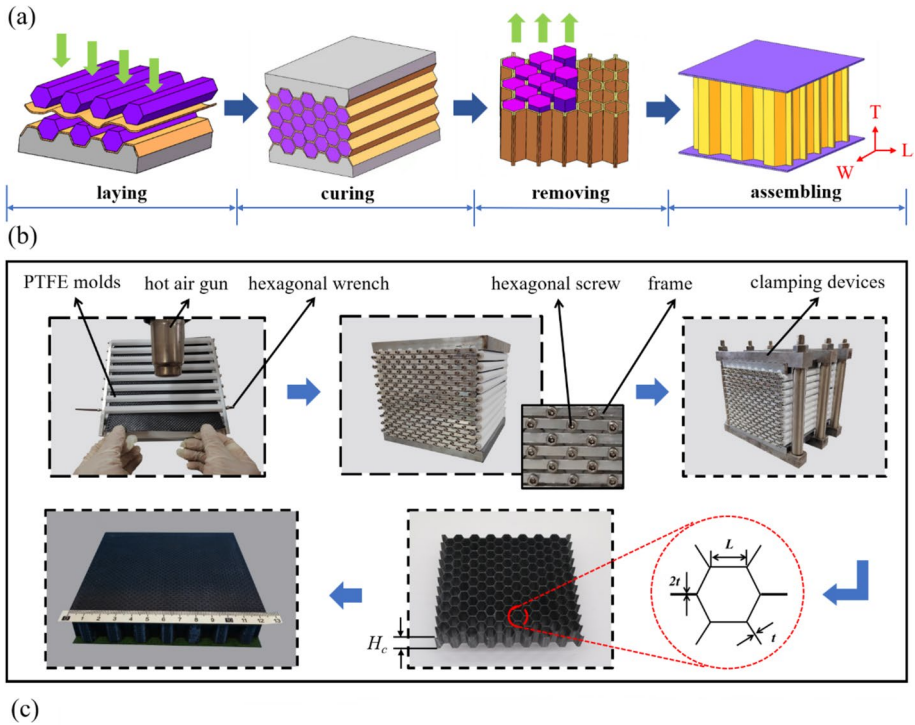| E_{11} (Gpa)	E_{22} (Gpa)	E_{33} (Gpa)	G_{12} (Gpa)	G_{13} (Gpa)	G_{23} (Gpa)
49.9	53.6	8.5	3.2	2.9	2.9
X_c (MPa)	Y_c (MPa)	Z_c (MPa)	X_t (MPa)	Y_t (MPa)	Z_t (MPa)
552.3	480.7	500	540.7	594.0	150
S_{12}	S_{13}	S_{23}	v_{12}	v_{13}	v_{23}
64.6	50	50	0.1	0.25	0.25

Fig. 1 Preparation process: **a** Schematic diagram of the preparation process, **b** Preparation process of honeycomb panels, **c** Sample images of carbon fiber composite honeycomb panels

replenishment instrument was used to control the electric blanket to be heated. The curing curve was shown in Fig. 2(b). First, the temperature rose to 126 °C at the rate of 3 °C/min. When the temperature reached 126 °C, it was maintained for 90 min. Finally, cooling to 30 °C at a rate of 2 °C/min.

The cores were prepared by the hot press molding method. Through the regular array discharge of the PTFE molds, the interval fitting parts of the prepreg were bonded to each other. Then, it was placed in the autoclave for heating and pressing to form a honeycomb core at one time. There were four main steps: laying, curing, removing, and assembling, as shown in Fig. 1(b). Finally, the face sheets and the core were bonded using the modified epoxy adhesive film (METLBOND® 1515-4 M) from Solvay. The CFCHs were obtained by secondary curing [33].
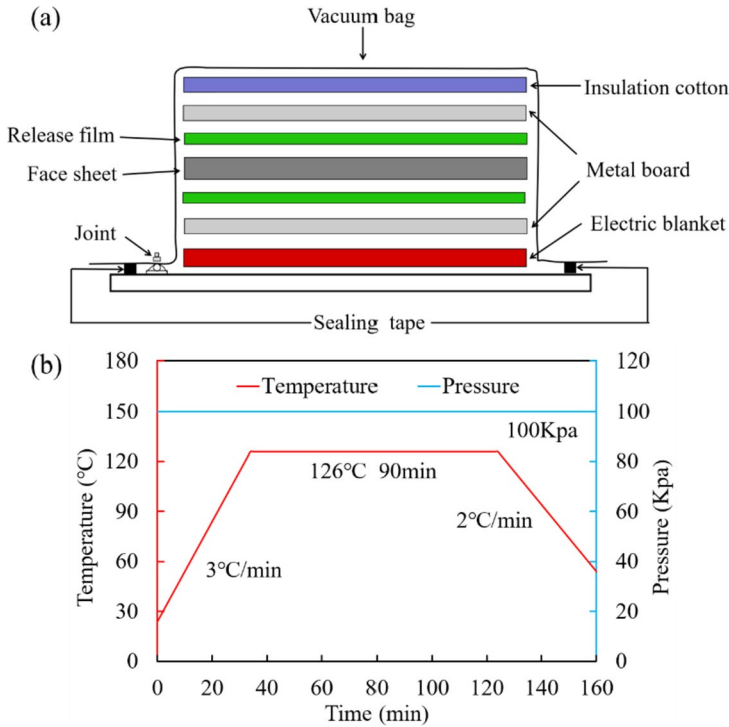
Fig. 2 Fabrication process of composite face sheets: **a** Face sheets preparation schematic, **b** Curing curve

2.2 Experimental Set-Up

Low-velocity impact experiments were carried out on an Instron CEAST 9350 drop weight testing machine, as shown in Fig. 3. The facility was equipped with a crosshead, a tup holder, a rebound brake, and an impactor instrumented with a force transducer. The force transducer had a maximum range of 45 kN, and the data acquisition frequency was 10^6 Hz. The impactor used in the experiments was a hemisphere with a diameter of 20 mm and a mass of 10.48 kg. The experiments were carried out according to ASTM D7136 [34]. The size of the specimen was approximately 120 mm×120 mm×22 mm, which was clamped by a pneumatic clamping fixture consisting of two cylindrical rings with an opening diameter of 76 mm. The applied air pressure was 0.6 Mpa. In these experiments, seven levels of impact energy (5 J, 10 J, 30 J, 50 J, 60 J, 70 J, and 100J) were tested. The impact force, displacement, and energy absorption were obtained through the supporting data acquisition system to study the dynamic responses of the CFCHs.

3 Result and Discussion

3.1 Force–Displacement Responses

Low-velocity impact experiments with different energies were conducted on CFCHs. The results indicate that the dynamic responses of CFCHs under low-velocity impact
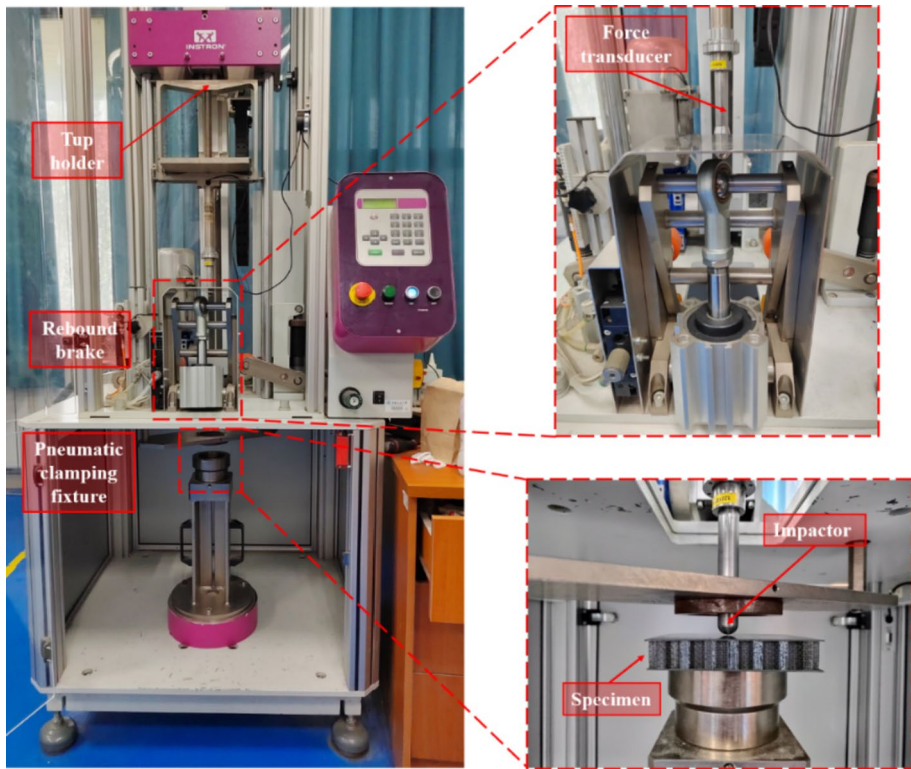
Fig. 3 Schematic of the low-velocity impact test setup

is consistent with that of aluminum honeycomb [35] and foam sandwich structures [36]. Under different energy impacts, the force–displacement curves show three typical modes, complete rebound (Type I), incomplete rebound (Type II), and partial or complete penetration (Type III), as shown in Fig. 4.

When the impact energy is 5J and 10J, the force–displacement curves show a single peak (Type I). As the displacement increases, the force grows linearly to the initial peak (F_0). Subsequently, the force increases to the first peak force (F_{max1}). At this time, the impactor reaches the maximum displacement. Finally, the impactor rebounds and the force drops to 0. In addition, the initial peak (F_0) and the first peak (F_{max1}) increase with the increase of impact energy. The fluctuation growth stage also becomes longer.

When the impact energy is 30 J and 50 J, the force–displacement curves show a single peak and a force platform (Type II). The force increases rapidly to the F_{max1} and then decreases. As the impactor continues to move downward, the core absorbs a significant portion of the force, resulting in the curve entering a platform stage. The higher the impact energy, the higher the first peak force (F_{max1}) and the longer the platform.

When the impact energy is 60 J, 70 J, and 100J, the curves show the double peak (Type III). Once the impactor contacts the front face sheet, the force quickly rises, reaching the first peak force (F_{max1}). The contact force keeps decreasing as the damage enlargement of the front face sheet and the crushing of the honeycomb core by the impactor. Under the support of the back face sheet and the core, the force gradually increases again. Then, the
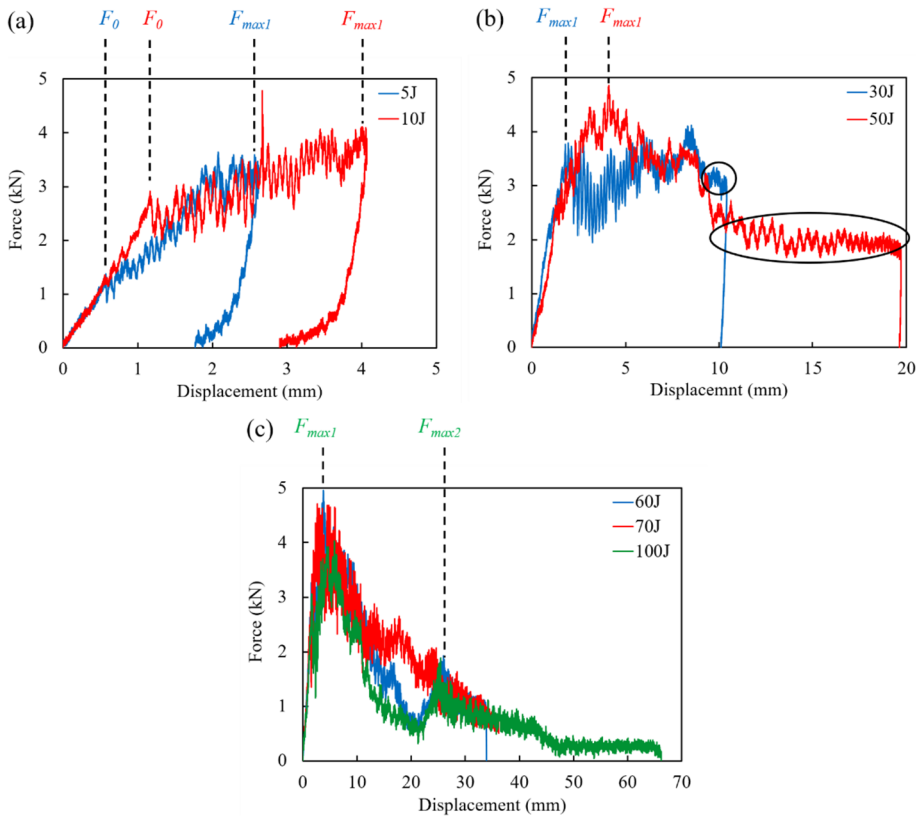
Fig. 4 Force–displacement curves under different impact energies: **a** Type I, rebound, **b** Type II, incomplete rebound, **c** Type III, partial or complete penetration

second peak force (F_{max2}) appears. It is worth noting that, unlike the F_{max1} of the impact responses of the metal honeycomb sandwich panel is slightly lower than the F_{max2} [35], the F_{max2} of the CFCHs is much smaller than the F_{max1}.

3.2 Deformation Mechanisms

In this section, three kinds of energies (10 J, 50 J, and 100J) are selected to analyze the three typical deformation mechanisms in detail, focusing on displacement and energy absorption. During impact, there is a significant vibration after contact, resulting in a violent oscillation of the curves, which have been smoothed to show the changing trend more clearly.

　As shown in Fig. 5, in the initial stage of loading, the force increases linearly with time while the energy rises slowly. The initial force (F_0) at t_0, which is called critical damage threshold load [37], is usually used to characterize the damage impedance capability of the composite. As the loading continues, delamination occurs on the front face sheet and spreads rapidly [38], causing a reduction in the stiffness of the specimen. Then, invisible fiber breakage and matrix cracking occur on the face sheet. The force increases to the F_{max1}. With the increase of impact displacement, the face sheet/core interface is damaged. During this process, the energy absorption increases rapidly. The maximum displacement

(D_{max}) and the peak energy absorption (E_{max}) are reached at t_3, which signifies the end of the loading stage. Finally, the impactor begins to rebound. A part of the energy is converted into the kinetic energy of the impactor through the elastic energy (E_{max}-E_a), while the remaining energy (E_a) is absorbed through different damage modes and friction.

The response curve of CFCHs at 50 J impact energy is shown in Fig. 6. In the initial stage, the force increases linearly, reaching the F_{max1} at t_1. With the increase of the impact process, the front face sheet cracks. The progressive folding deformation mechanisms of the honeycomb cell wall causes the curve to take on a platform stage. At t_3, the displacement of the impactor is the largest. The CFCHs absorb almost all the energy. The energy and displacement curves are parallel to the time axis. The impactor hardly rebounds. In general, when the honeycomb panel is subjected to medium energy impact, the face sheet and the core suffer apparent damage. Most of the energy is absorbed irreversibly, and only a small part is converted into the kinetic energy of the impactor during the rebound process.

It can be found from Fig. 7 that when the impactor hits the panel with high energy, the force increases rapidly and reaches the F_{max1} at t_1. Then, the force drops to a trough as a result of fiber breakage and crack propagation. At the same time, the core undergoes buckling and crushing deformation. With the combined action of the friction between the impactor and the panel, the force reaches the second peak force (F_{max2}) at t_2. Finally, the force drops to close to 0 and the honeycomb panel is completely penetrated. The difference is that the displacement increases almost linearly at high energy impact. When the impact energy is 100J, the energy absorption curve can be divided into two stages [35]. In each stage, the energy-time curve first rises slowly. As the contact area between the impactor and the face sheet increases, damage such as fiber breakage continues to occur and expand. The curve rises rapidly. Finally, the material has suffered severe damage, resulting in a slow increase in the curve.
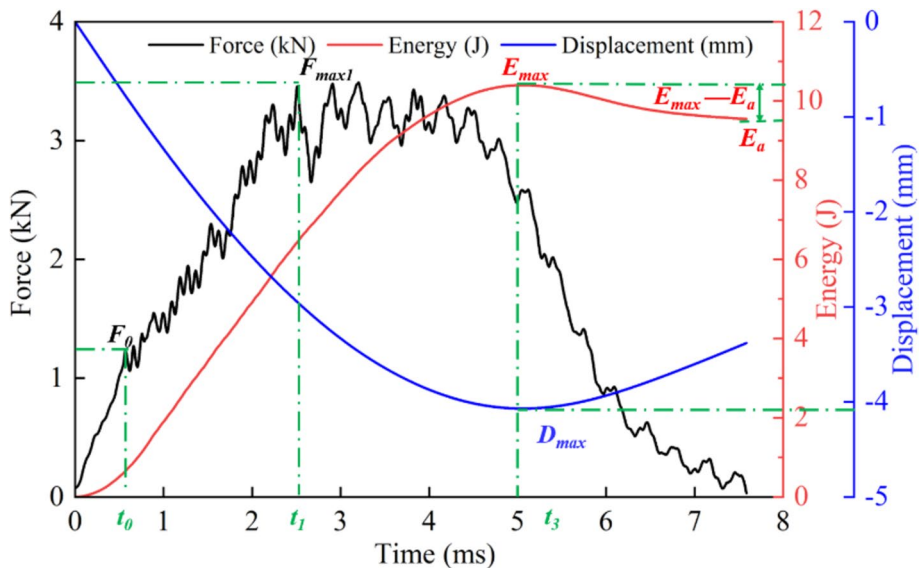

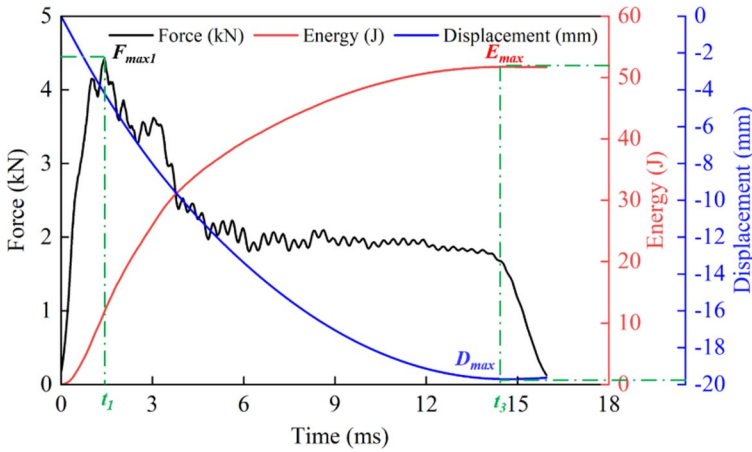**Fig. 5** Response curves of CFCHs under 10J impact energy

Fig. 6 Response curves of CFCHs under 50J impact energy

3.3 Failure Modes

The damage morphology of the face sheets and the cores after different energy impacts is shown in Fig. 8. When the impact energy is 5 J, the front face sheet produces a pit with a width of about 11 mm. From the cross section, it is found that the front face sheet appears delaminated. As the impact energy increases to 10 J, the width of the damaged area expands to 14 mm, accompanied by significant fiber breakage and matrix cracking.

When the impact energy is medium (30J and 50J), a circular hole of approximately 20 mm diameter is formed on the front face sheet, with no visible damage to the back face sheet. At an impact energy of 30J, the fiber undergoes tensile failure. Four fragments of almost equal size are formed, which is the same as the failure modes of the carbon-fiber foldcore sandwich structure under impact load in Ref. [31]. At an impact energy of 50 J, a complete fragment is created in the hole. The cell wall shows significant buckling.
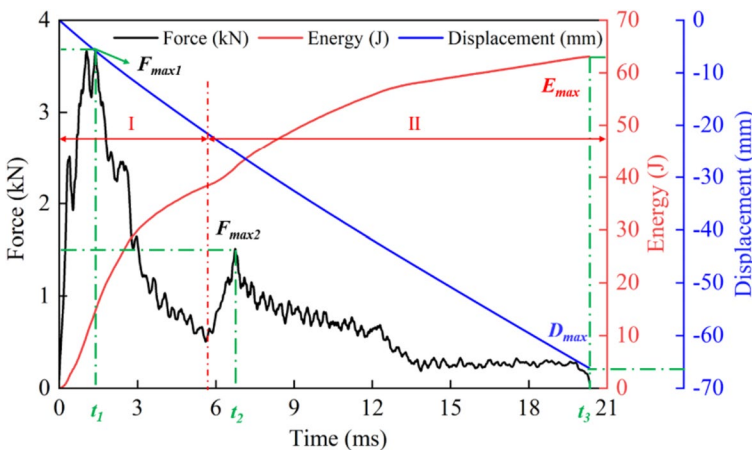

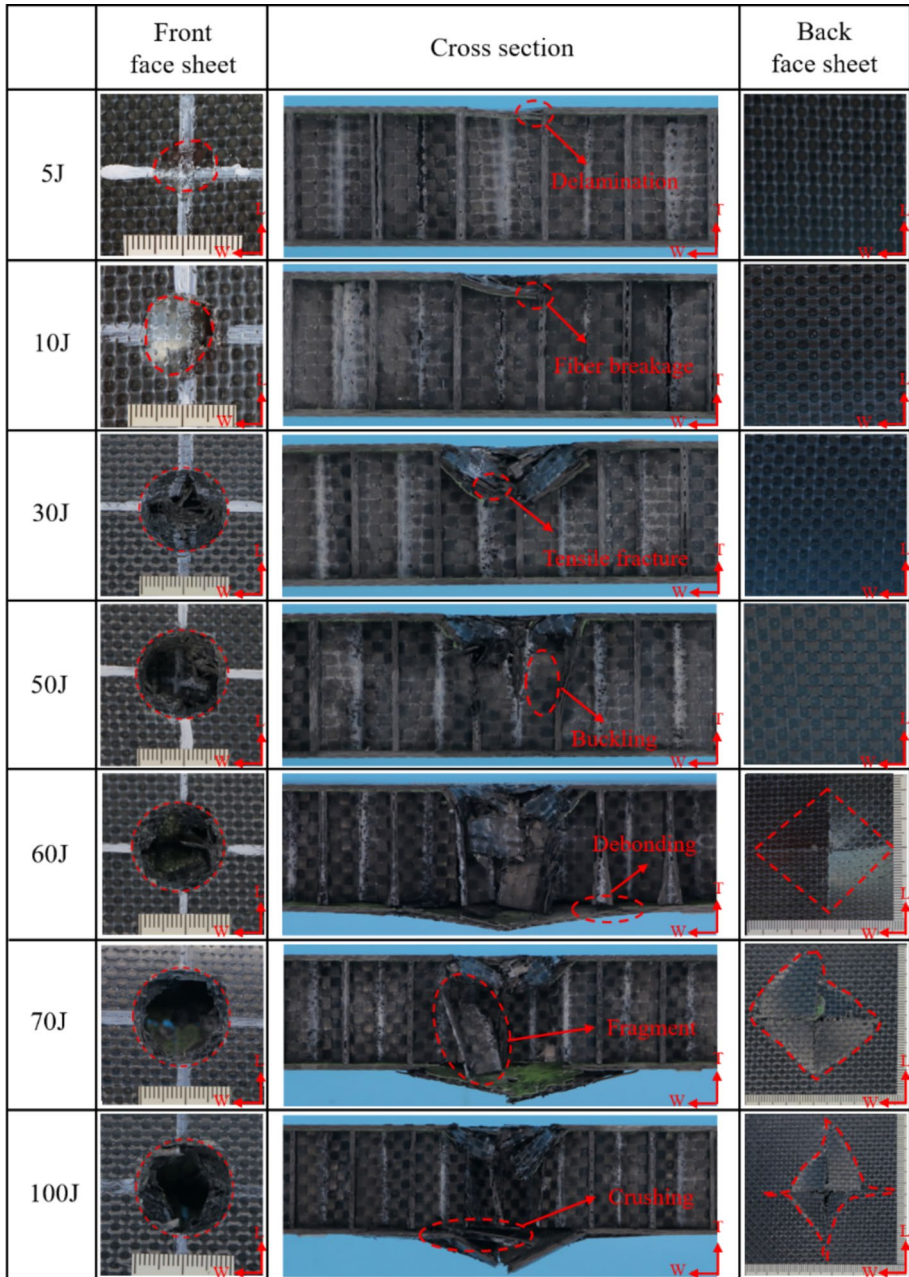**Fig. 7** Response curves of CFCHs under 100J impact energy

Fig. 8 The damage morphology of CFCHs under different impact energies

When the impact energy is high (60J, 70J, and 100J), the front face sheet produces a circular punching hole with a diameter similar to that of the impactor. The damage of the punching edge is similar to the shear fracture that occurred when a 3D printed part failed

[39]. the back face sheet has significant damage. at an impact energy of 60 J, two cracks of around 43 mm and 50 mm are produced on the back face sheet, developing along the weave of the fiber [40]. at an impact energy of 70 J, the damaged area of the back face sheet can be regarded as a square consisting of four triangles. Both cracks are about 45 mm. Besides, the core undergoes crushing failure with a large number of fragments. At an impact energy of 100 J, the panel is fully penetrated, with cracks extending up to 60 mm along the sides of the triangle. From the cross section, it is found that the back face sheet is severely delaminated. The actual damage area is larger than the actual visible area [41].

4 Finite Element Analysis

4.1 Material Model

The progressive damage behavior of honeycomb sandwich panels was simulated by VUMAT. The strain-based failure criterion of composite fabric [42] and Yeh criterion [43] were used to predict the damage and delamination failure, respectively. The progressive damage model consists of the following failure modes:

Tensile failure in fiber direction:

$$F_{xt} = (\frac{\varepsilon_{11}}{Y_T^\varepsilon})^2 + (\frac{\gamma_{12}}{S_{12}^\varepsilon})^2 + (\frac{\gamma_{13}}{S_{13}^\varepsilon})^2, \ \varepsilon_{11} \geq 0 \tag{1}$$

Compressive failure in fiber direction:

$$F_{xc} = (\frac{\varepsilon_{11}}{X_C^\varepsilon})^2, \ \varepsilon_{11} \leq 0 \tag{2}$$

Tensile failure in transverse direction:

$$F_{yt} = (\frac{\varepsilon_{22}}{Y_T^\varepsilon})^2 + (\frac{\gamma_{12}}{S_{12}^\varepsilon})^2 + (\frac{\gamma_{13}}{S_{13}^\varepsilon})^2, \ \varepsilon_{22} \geq 0 \tag{3}$$

Compressive failure in transverse direction:

$$F_{yc} = (\frac{\varepsilon_{11}}{Y_C^\varepsilon})^2, \ \varepsilon_{22} \leq 0 \tag{4}$$

Yeh delamination failure:

$$F_{dl} = (\frac{\varepsilon_{33}}{Z_T^\varepsilon})^2 + (\frac{\gamma_{13}}{S_{13}^\varepsilon})^2 + (\frac{\gamma_{23}}{S_{23}^\varepsilon})^2, \ \varepsilon_{33} \geq 0 \tag{5}$$

where X_T^ε and Y_T^ε are the tensile failure strains in the longitudinal and latitudinal directions, X_C^ε and Y_C^ε are the compressive failure strains in the longitudinal and latitudinal directions respectively. Z_T^ε is the out-of-plane tensile failure strain.

In this paper, the damage accumulation is defined by introducing damage variable d_i ($i = xt$, xc, yt, yc, dl), and a three-dimensional progressive damage model for composites is established.

$$d_i = 1 - \exp\left[\frac{1}{m_i}\left(1 - (F_i)^{m_i}\right)\right], \; F_i \geq 1 \tag{6}$$

where m_i ($i = xt, xc, yt, yc, dl$) is the material softening parameter. The larger the value of m_i, the faster the rate of stiffness decay of the material. The material softening parameters chosen in this paper are 0.01, 0.008, 0.01, 0.008, and 0.15. And the incremental damage variables simulate the extension of the damage:

$$d_i^t = \max\left\{0, d_i^\tau\right\}, (\tau \leq t; i = xt, xc, yt, yc, dl) \tag{7}$$

where d_i^t is the damage variable at the current moment.

The stiffness decay of the material after unit failure is achieved with the damage parameter ω_j ($j = 1, 2\ldots6$), which can be calculated using the damage variable d_i.

$$\begin{aligned}
\omega_1 &= \max\left\{0, d_x\right\} \\
\omega_2 &= \omega_4 = \max\left\{0, d_x, d_y\right\} \\
\omega_3 &= \omega_5 = \omega_6 = \max\left\{0, d_x, d_{dl}\right\}
\end{aligned} \tag{8}$$

where $d_x = \max\left\{0, d_{xt}, d_{xc}\right\}$, $d_y = \max\left\{0, d_{yt}, d_{yc}\right\}$.

The constitutive model of the composite after stiffness decay is:

$$\varepsilon = S_d \bullet \sigma \tag{9}$$

where $\boldsymbol{\varepsilon} = [\varepsilon_{11}, \varepsilon_{22}, \varepsilon_{33}, \gamma_{12}, \gamma_{23}, \gamma_{13}]^{\mathrm{T}}$, $\boldsymbol{\sigma} = [\sigma_{11}, \sigma_{22}, \sigma_{33}, \tau_{12}, \tau_{23}, \tau_{13}]^{\mathrm{T}}$.

$$S_d = \begin{bmatrix}
\frac{1}{E_{11}(1-\omega_{11})} & -\frac{v_{12}}{E_{22}} & -\frac{v_{13}}{E_{33}} & 0 & 0 & 0 \\
-\frac{v_{12}}{E_{22}} & \frac{1}{E_{22}(1-\omega_2)} & -\frac{v_{23}}{E_{22}} & 0 & 0 & 0 \\
-\frac{v_{13}}{E_{33}} & -\frac{v_{23}}{E_{22}} & \frac{1}{E_{33}(1-\omega_3)} & 0 & 0 & 0 \\
0 & 0 & 0 & \frac{1}{G_{12}(1-\omega_4)} & 0 & 0 \\
0 & 0 & 0 & 0 & \frac{1}{G_{23}(1-\omega_5)} & 0 \\
0 & 0 & 0 & 0 & 0 & \frac{1}{G_{13}(1-\omega_6)}
\end{bmatrix} \tag{10}$$

4.2 Finite Element Model

Based on Abaqus/Explicit modeling and simulation software, the finite element model of hemispherical impactor impacting CFCHs was established. The model consisted of honeycomb panel, clamps, and impactor, as depicted in Fig. 9. The impactor was meshed by R3D4 element, while the clamps and honeycomb panel were meshed by three-dimensional solid element C3D8R with hourglass control.

The mesh convergence analysis of the impact responses and computing time of composite honeycomb panels under the impact energy of 100J was carried out, as shown in Fig. 10. Mesh sizes of 2 mm, 1 mm, 0.8 mm, 0.5 mm, and 0.3 mm were chosen. With the refinement of the mesh, it could be found that the force and maximum displacement converged to stable values, but the computing time increased. In summary, the simulation results tended to converge when the mesh size of the square area of the impact
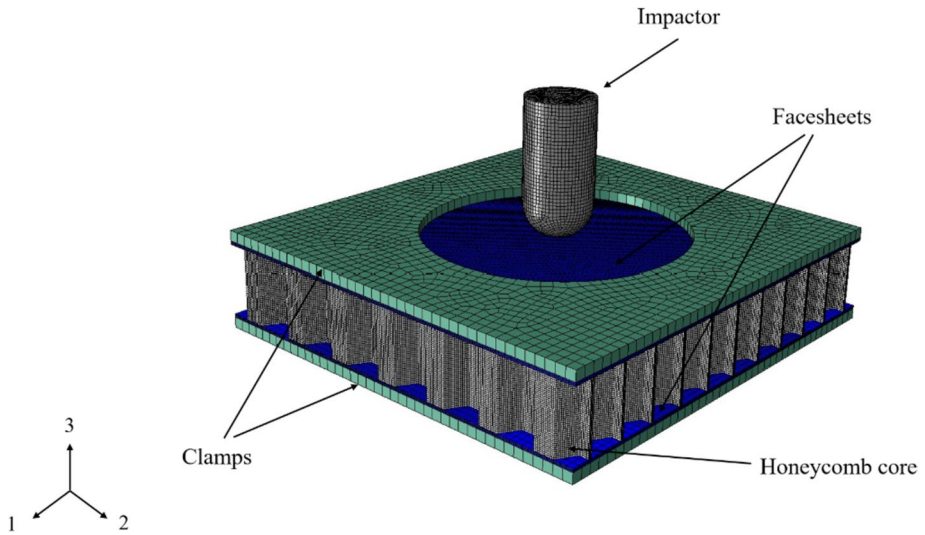
Fig. 9 Full-scale FE model of a honeycomb-core sandwich panel under impact loading

region was $0.5\ \text{mm} \times 0.5\ \text{mm}$. The results also matched the experimental results with small relative error.

In the finite element model, the material properties of carbon fiber/epoxy prepreg are shown in Table 1. The clamps were simulated with steel, and the material parameters are shown in Table 2. Besides, the top clamp was only allowed to move in the 3-direction. The bottom clamp was fully constrained in displacement and rotation. The "tie" constraint was used between the clamp and honeycomb panel, ignoring the initial clamping pressure. The motion of the impactor was controlled by a reference point created in the discrete rigid that had only one translational degree of freedom along the 3-direction. The total mass and the initial impact velocity were assigned to this reference point in the impactor.
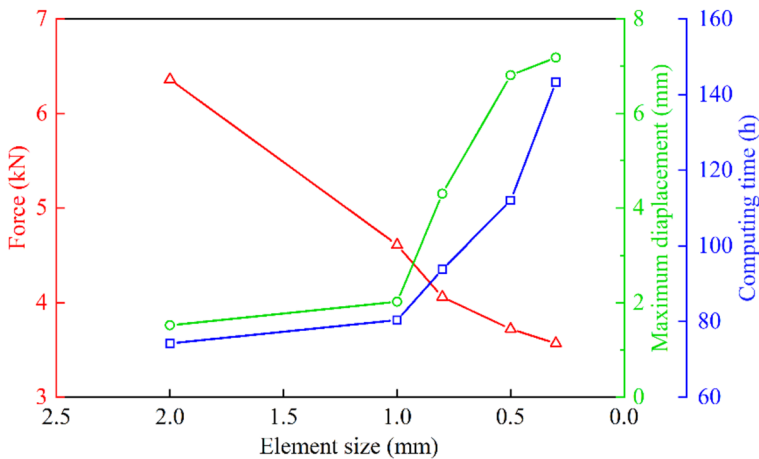

Fig. 10 Mesh convergence analysis: effect of element size on the impact response and computing time

Table 2 Material properties of the steel [17]	Elastic modulus (*E*)	Poisson ratio (*v*)	Density (*ρ*)
	210 Gpa	0.3	7.8×10^{-9} t/mm^3

Since debonding of the specimens did not occur after the experiments, the tie connection was used between the face sheet and the core. The general contact definition was used to define the interaction between the impactor and each layer of the honeycomb panels. The normal interaction was hard contact, and the tangential interaction was set with a friction coefficient of 0.2. Self-contact algorithm was used to define possible contact among the cell walls to prevent the interpenetration between the folds in the honeycomb walls during impact [44].

4.3 Finite Element Model Validation

Figure 11(a) shows a comparison of experiments and simulation results on force–displacement curves for CFCHs under 100J impact energy. The simulation effectively predicts the double peak of the curve. Features such as the slope of the linear part, the first peak force (F_{max1}), and load fluctuations can be adequately captured. However, the predicted second peak force (F_{max2}) is slightly higher than the actual. In addition, it can be found from Fig. 11(b) that the simulated and experimental results are in good agreement with the failure modes. In Fig. 11(c) and (d), the error in the simulation for the residual velocity and energy is 9.68% and 7.37%, which is acceptable for a non-linear dynamic analysis. The results show that the numerical model developed for the composite honeycomb panels is sufficiently accurate to be used for analysis instead of the actual prototype.
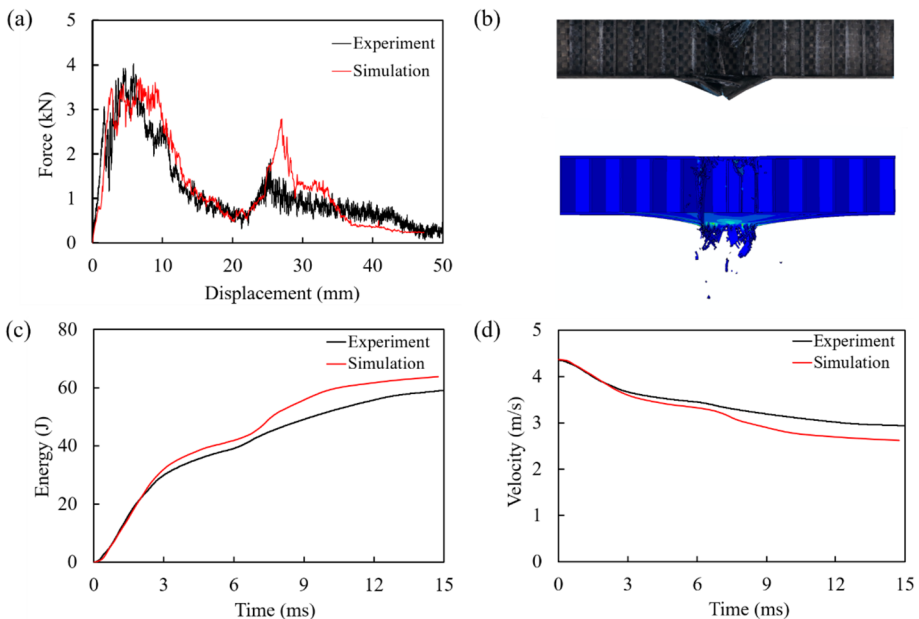

Fig. 11 The results of experiments and simulation (100J): **a** Histories of force and displacement, **b** Typical predicted damage modes, **c** Histories of velocity and time, **d** Histories of energy and time
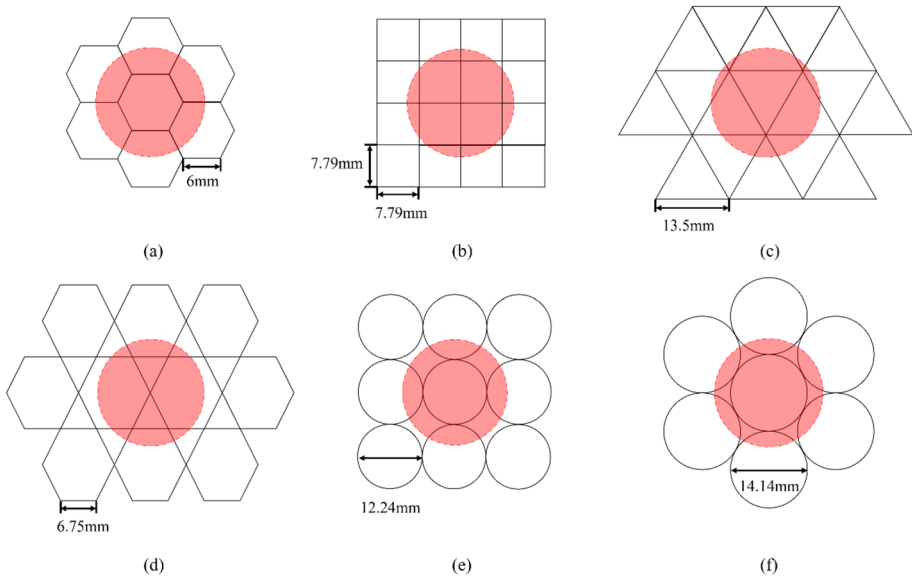
Fig. 12 Schematic diagram of different honeycomb structures, **a** hexagonal honeycomb, **b** square honeycomb, **c** triangular honeycomb, **d** Kagome honeycomb, **e** circular honeycomb in square arrangement (CS type), **f** circular honeycomb in hexagonal arrangement (CH type)

5 Comparison of Different Honeycomb Configurations

5.1 Configuration Design

In this paper, the low-velocity impact performance of six different honeycomb configurations under 100J is analyzed by the finite element model. Figure 12 shows the different honeycomb configurations, where the red area represents a circular impact area with a diameter of 20 mm (the same as the impactor diameter). Hexagonal, square, triangle, and Kagome are all regular polygons. The two types of circle honeycombs can be divided into square arrangement (CS type) and hexagonal arrangement (CH type) [45].

Before performing the finite element analysis, the parameter design is first completed so that the relative densities of each honeycomb panel are equal. All unit cells have a stacking

Table 3 Parameters of different honeycomb configurations [29]

Core configuration	Thickness t (mm)	Side length l (mm)	Relative density $\bar{\rho}$
Hexagonal honeycomb	$t = 0.5$	$l_h = 6$	$\bar{\rho} = \frac{8}{3}\frac{t}{l_h\sqrt{3}}$
Square honeycomb		$l_s = 7.8$	$\bar{\rho} = \frac{2t}{l_s}$
Triangular honeycomb		$l_t = 13.5$	$\bar{\rho} = \frac{2\sqrt{3}\cdot t}{l_t}$
Kagome honeycomb		$l_k = 6.75$	$\bar{\rho} = \sqrt{3}\frac{t}{l_k}$
Circular honeycomb (CS type)		$l_{sc} = 12.24$	$\bar{\rho} = \pi\frac{t}{l_{cs}}$
Circular honeycomb (CH type)		$l_{ch} = 14.14$	$\bar{\rho} = \frac{2\sqrt{3}\pi\cdot t}{3l_{ch}}$

sequence of [0°/90°] with a wall thickness of 0.5 mm. By adjusting the side length, the relative density of other honeycomb configurations is 12.83%, which is the same as that of the hexagonal honeycomb. The specific parameters are shown in Table 3.
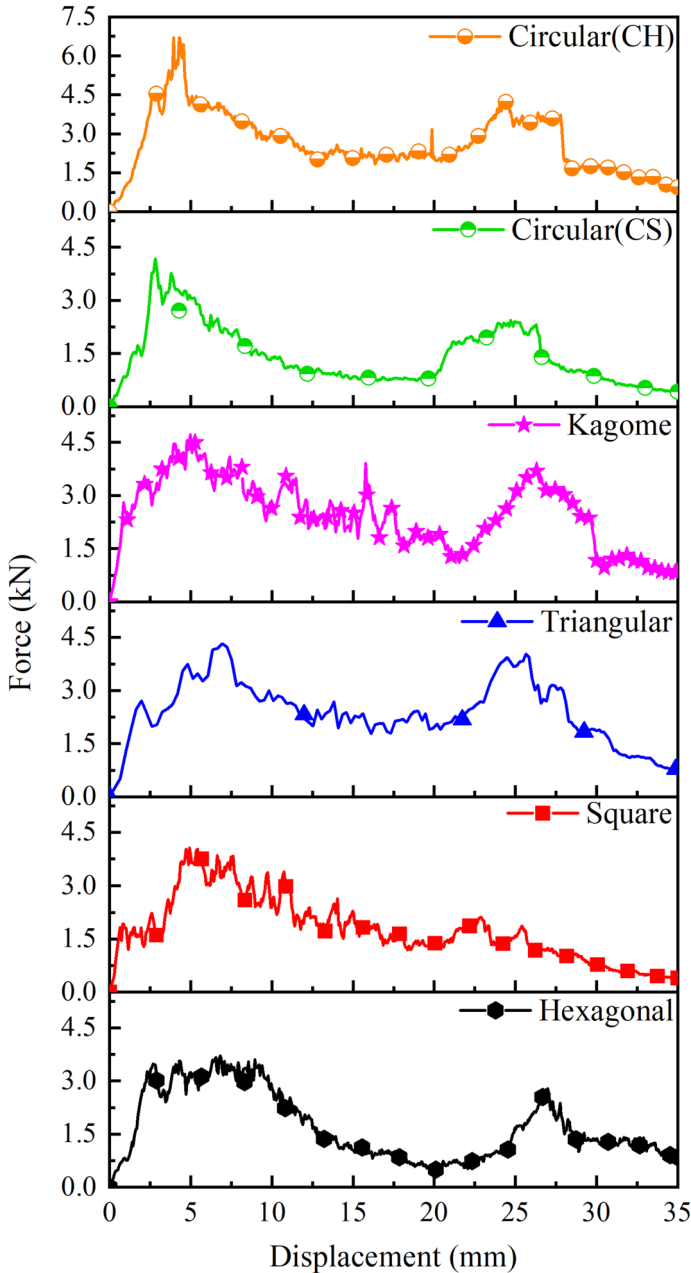

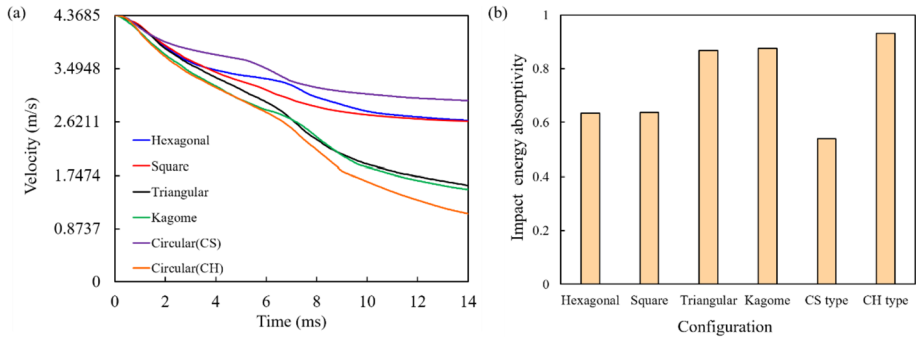**Fig. 13** Force–displacement curves of different honeycomb configurations

Fig. 14 Mechanical properties response curve: **a** Velocity–time curve, **b** Impact energy absorptivity of different honeycomb configurations

5.2 Low-Velocity Impact Properties

The force–displacement curves of all different honeycomb panels show the double peak (Type III), as shown in Fig. 13. The F_{max1} and F_{max2} of the circular honeycomb (CH type) are the largest. This is because the number of circular honeycomb edges is large. The axial cracks generate during the impact process increase, resulting in higher crushing strength [46]. The F_{max1} of the Kagome honeycomb is second only to that of the circular honeycomb (CH type), while the hexagonal honeycomb has the smallest F_{max1}. For other honeycombs, the F_{max1} is roughly equal.

From the velocity–time curve in Fig. 14(a), it can be seen that the velocity of impactor begins to decrease from 4.3685 m/s at the first 1 ms. However, the Kagome and circle honeycombs (CH type) decrease faster. In 2-6 ms, the impactor contacts the core. The velocity decreases slowly. After 6 ms, the back face sheet is broken down. The residual velocities of the circular (CS type), hexagonal, and square honeycombs are 2.966 m/s, 2.646 m/s, and 2.630 m/s, respectively. They are all higher than the residual velocity of the Kagome and triangular honeycombs, which are 1.544 m/s and 1.583 m/s. The circular honeycomb (CH type) has the smallest residual velocity at 1.442 m/s, which can be attributed to its unique honeycomb configuration and the particular properties of arrangement. This high peak force and low residual velocity are allowed for practical applications in aerospace and engineering, where high impact resistance and energy absorption are crucial.

To compare the energy absorption capacity of panels with different configurations, the calculation formula of energy absorption (EA) is as follows:

Table 4 Parameters of different honeycomb configurations

Core configuration	F_{max1} (kN)	F_{max2} (kN)	Energy absorption (J)
Hexagonal honeycomb	3.715	2.792	63.335
Square honeycomb	4.063	2.115	63.744
Triangular honeycomb	4.320	4.025	86.865
Kagome honeycomb	4.721	3.725	87.514
Circular honeycomb (CS type)	4.183	2.437	53.899
Circular honeycomb (CH type)	6.714	4.404	93.139

$$EA = \frac{1}{2}M(v_0^2 - v_r^2)$$

where M is the mass of impactor, v_0 is the initial velocity, and v_r is the residual velocity after impact. The results of EA are listed in Table 4. It is evident that the circular honeycomb (CH type) exhibits the highest energy absorption capacity. Compared with other honeycomb configurations, the circular unit cell has no sharp edges and corners, which avoids stress concentration [47]. Besides, the unit cell of CH type has more constraints than the unit cell of CS type, resulting in a shorter length of cell wall buckling folds and increased energy absorption [45].

The energy absorptivity is also compared, as shown in Fig. 14(b). The energy absorptivity is the ratio of EA to the kinetic energy before impact. Different from the conclusion that the energy absorption increases with the increase of the number of unit cell edges in quasi-static compression [48], the energy absorption of triangular honeycomb is greater than that
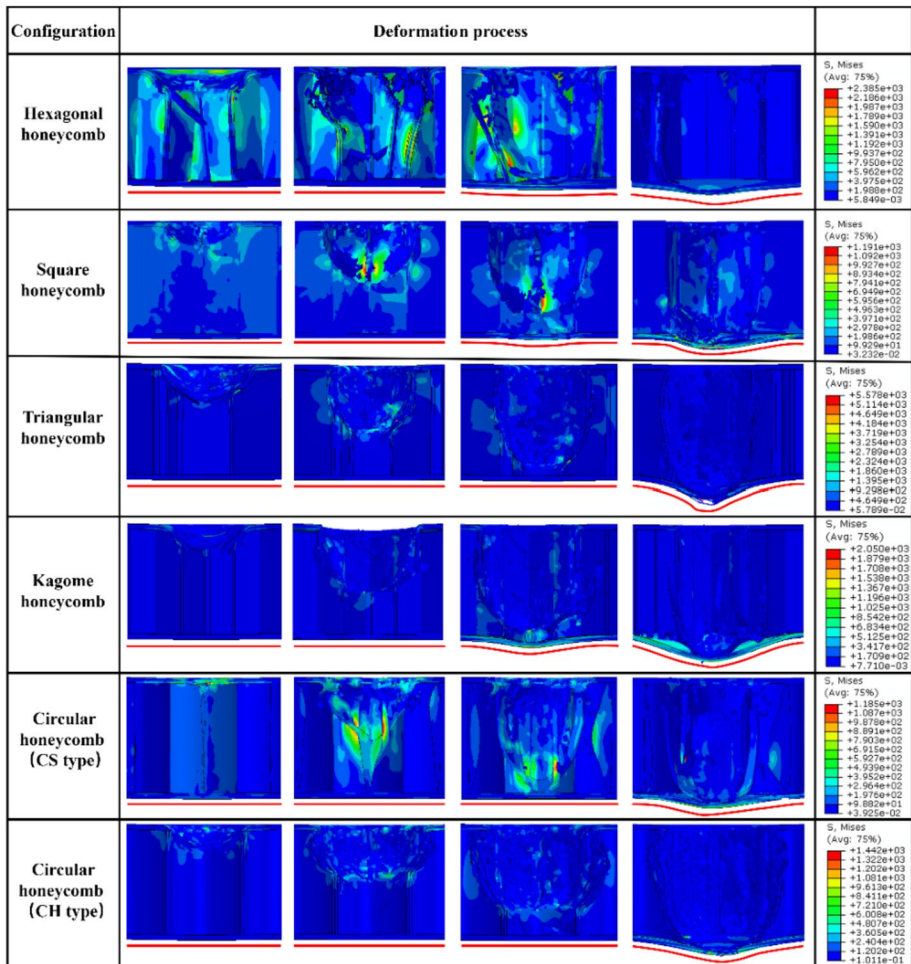

Fig. 15 The deformation process of honeycomb cross section view during the simulation: impact energy 100J
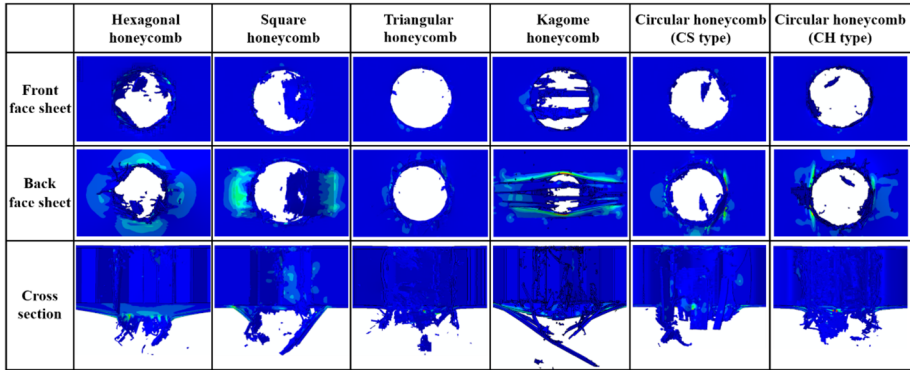
Fig. 16 Numerical simulated damage of different honeycomb configurations after low-velocity impact

of square honeycomb and hexagonal honeycomb in low-velocity impact experiments. This phenomenon also appears in Ref. [49].

5.3 Deformation Modes

Figure 15 shows the deformation process of different honeycomb panels when the force is between the F_{max1} and F_{max2} during the simulation. The cell walls of hexagonal, square, and circular honeycombs (CS type) have high stress during the impact progress. They are eventually crushed into fragments and do not completely fail, either remaining within the unit cell or flying out with the impactor. As a result, these three configurations exhibit poor effectiveness in energy absorption. However, the stress of other honeycombs is concentrated more specifically at the contact position between the impactor and the honeycomb core. The core exhibits characteristics of progressive crushing failure. Due to the serious damage of carbon fiber, some failure units are removed and pits are formed in the core. Subsequently, the damage expands in the direction of impact. When the force
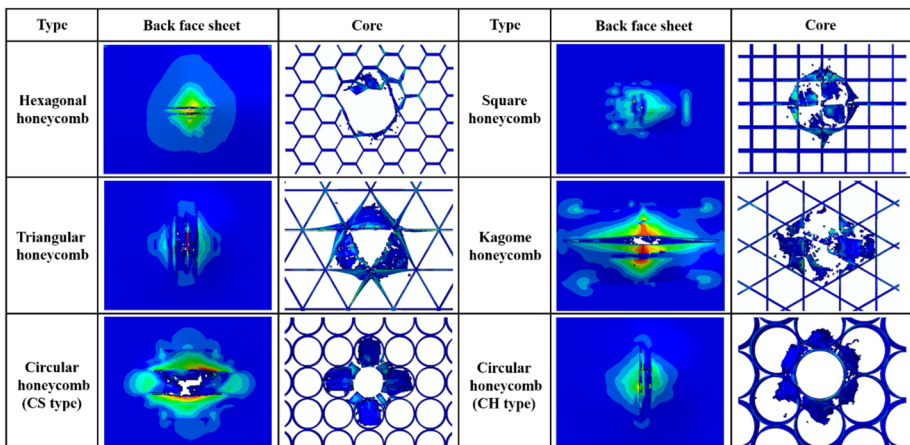

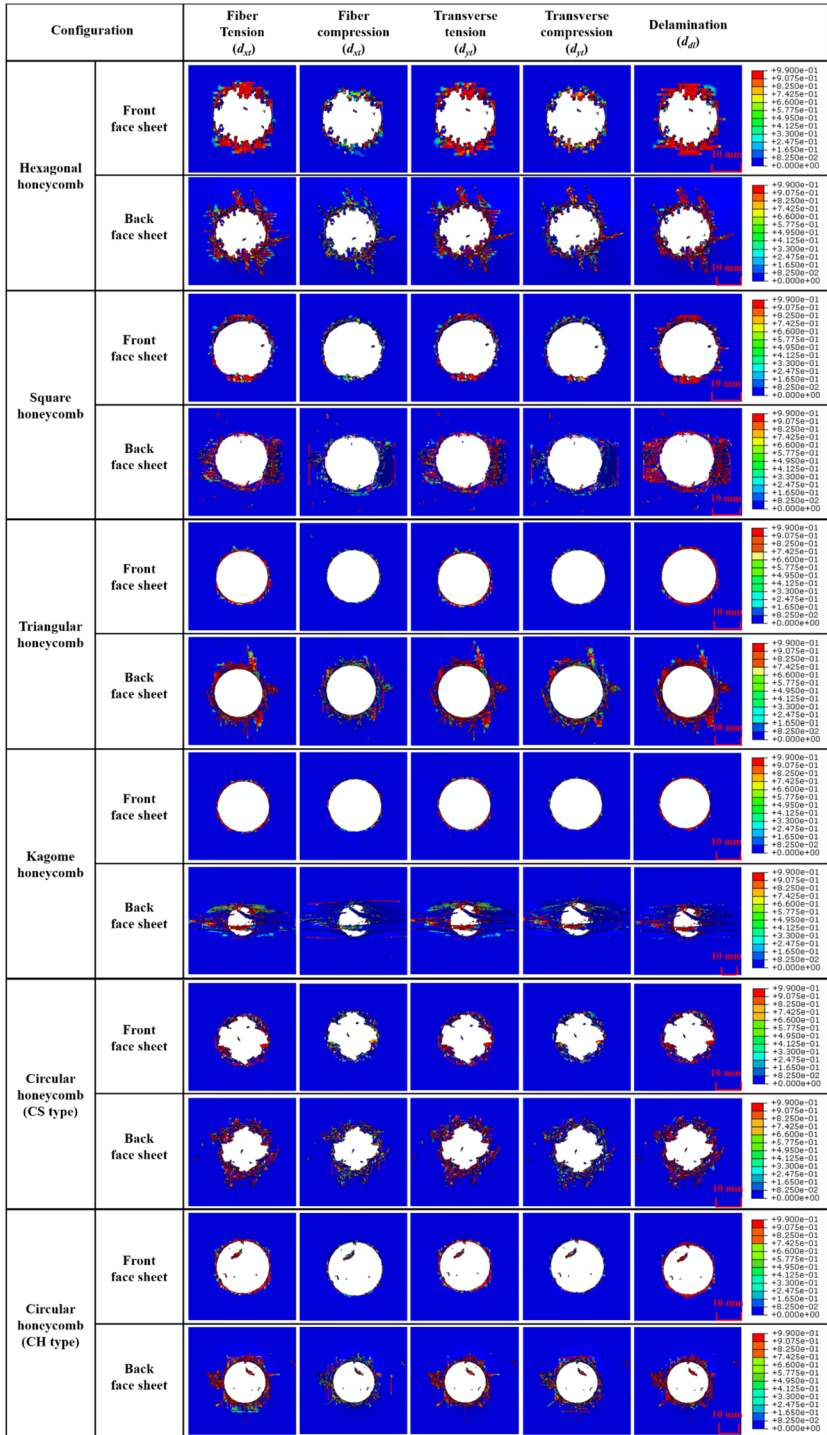**Fig. 17** Numerical simulated damage of honeycomb core and back face sheets at F_{max2}

Fig. 18 Typical predicted damage modes of composite face sheets under the impact energy of 100J
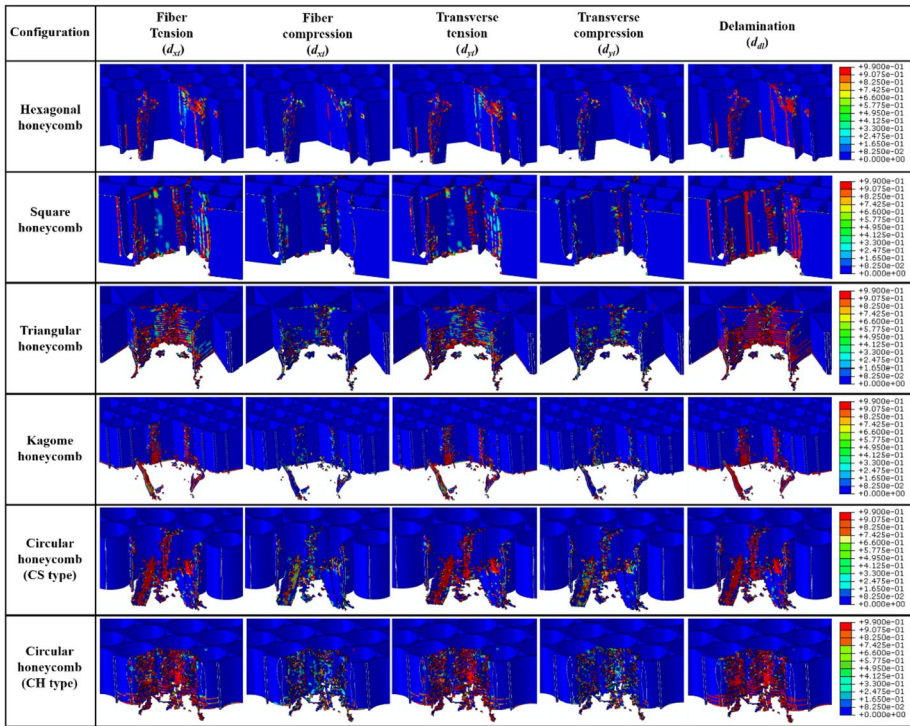
Fig. 19 Typical predicted damage modes of composite honeycomb cores under the impact energy of 100J

reaches the F_{max2}, the Kagome and triangular honeycombs exhibit more significant local deformation on their back face sheet than other honeycombs.

The damage morphology of the six honeycomb configurations after low-velocity impact is shown in Fig. 16. It is found that the back face sheet of the square honeycomb produces square fragments. In contrast, the Kagome honeycomb undergoes fiber tensile tearing damage. Other honeycombs produce circular holes on the back face sheet.

By analyzing the damage modes of the core and back face sheets at F_{max2}, the mechanical properties of different configurations are compared, as shown in Fig. 17. The back face sheets of square honeycomb, Kagome honeycomb, and circular honeycomb (CS type) show a rectangular damage profile, with the damage expanding mainly in the direction of the long side parallel to the rectangle. In contrast, the back face sheets of other honeycombs deforms approximately to a circular bulge.

Figure 18 shows typical predicted damage modes of face sheets under the impact energy of 100J, respectively. A circular damaged area is exhibited on the front face sheets. The size of the compression damage area is similar to the diameter of the impactor. Besides, the damaged scope of fiber and transverse tension failure is greater than that of fiber and transverse compression failure. It is worth noting that the area of compression failure and delamination of the back face sheets is significantly larger than that of the front face sheets.

Typical predicted damage modes of composite honeycomb cores are shown in Fig. 19. Compared with other honeycomb configurations, the degree of fragmentation

is higher for triangular and circular honeycomb cores, which results in more energy absorption. Different from the core damage of other honeycomb configurations limited to the impact area, the damage at the contact position between the Kagome honeycomb core and the back face sheet extends to several nearby cells.

6 Conclusion

In this paper, the low-velocity impact behavior of carbon fiber composite honeycombs was studied experimentally and numerically. The following conclusions can be drawn.

The force-displacement curves of carbon fiber composite honeycombs under low-velocity impact shows three typical modes, single peak, single peak followed by a platform, and double peak. They correspond to the three deformation modes of impactor rebound, incomplete rebound, and complete penetration of the composite honeycomb panels, respectively.

Under 100J impact, the first peak force and second peak force of circular honeycomb (CH type) are greater than other honeycomb configurations, absorbing the most energy. The energy absorption of the Kagome honeycomb and triangular honeycomb is close, which is about 40% more than that of hexagonal honeycomb and square honeycomb. The energy absorption of the circular honeycomb (CS type) is only 68% of that of the circular honeycomb (CH type), which proves that different arrangement layouts have different performances.

After impact, the back face sheet of the square honeycomb produces square fragments. The Kagome honeycomb forms tensile tearing damage, and the back face sheets of the hexagonal, triangular, and circular honeycombs (CS and CH types) appear circular holes.

Considering the labor and cost, only hexagonal honeycomb panels are prepared in this paper. Other honeycomb panels are modeled and studied by simulation. In addition, the responses of honeycomb sandwich panels with different cell configurations under different impact conditions, such as impactor shape and impactor diameter, deserves further discussion.

Author Contributions Yunfei Deng: Funding acquisition, Project administration, Supervision, Resources. Xiaoyu Hu: Investigation, Conceptualization, Mechanical tests, Data analysis, Writing-original draft, Writing-review & editing. Yijie Niu: Mechanical tests, Data analysis. Yimei Zheng: Project funding, Supervision. Gang Wei: Experimental guidance, resources.

Data Availability The raw data used to support the findings of this study are available from the corresponding author upon request.

Declarations

Ethical Approval The manuscript is original and has not been submitted for publication elsewhere (partially or in full). Also, the manuscript has not been submitted to more than one publication for simultaneous consideration.

Consent to Participate Not applicable (this research did not involve human subjects).

Consent to Publish The authors consent to the manuscript's publication in the ACMA should the article be accepted by the editor-in-chief upon completion of the refereeing process.

Competing Interest The authors have no relevant financial or non-financial interests to disclose.

References

1. Zhang, J.J., Lu, G.X., You, Z.: Large deformation and energy absorption of additively manufactured auxetic materials and structures: a review. Compos. B Eng. **201**, 108340 (2020). https://doi.org/10.1016/j.compositesb.2020.108340
2. de Souza, E.F., Gomes, G.F., Ancelotti, A.C., Jr., et al.: A numerical-experimental dynamic analysis of composite sandwich beam with magnetorheological elastomer honeycomb core. Compos. Struct. **209**, 242–257 (2019). https://doi.org/10.1016/j.compstruct.2018.10.041
3. Kösedağ, E., Ekici, R.: Free vibration analysis of foam-core sandwich structures Politeknik Dergisi. J. Polytech. **24**(1), 69–74 (2021). https://doi.org/10.2339/politeknik.571396
4. Rosmmi, N.H.M., Khan, Z.I., Mohamad, Z., et al.: Impact strength and morphology of sustainably sourced recycling polyethylene terephthalate blends. Chem. Eng. (2021). https://doi.org/10.3303/CET2183045
5. Wei, X.Y., Xiong, J., Wang, J., et al.: New advances in fiber-reinforced composite honeycomb materials. Sci. China Technol. Sci. **63**(8), 1348–1370 (2020). https://doi.org/10.1007/s11431-020-1650-9
6. Muhammed Raji, A., Hambali, H.U., Khan, Z.I., et al.: Emerging trends in flame retardancy of rigid polyurethane foam and its composites: a review. J. Cell. Plast. **59**(1), 65–122 (2023). https://doi.org/10.1177/0021955x221144564
7. Khosravani, M.R., Weinberg, K.: Experimental investigations of the environmental effects on stability and integrity of composite sandwich T-joints: experimentelle Untersuchung des Umwelteinflusses auf die Belastbarkeit von T-Stößen in Sandwich-Platten. Materialwiss. Werkstofftech. **48**(8), 753–759 (2017). https://doi.org/10.1002/mawe.201600747
8. Mohamad, Z., Raji, A.M., Hassan, A., et al.: Novel intumescent flame retardant of ammonium polyphosphate/sepiolite/melamine on rigid polyurethane foam: morphologies, and flammability properties. Chem. Eng. Trans. **89**, 619–624 (2021). https://doi.org/10.3303/CET2189104
9. Khan, Z.I., Habib, U., Mohamad, Z.B., et al.: Enhanced mechanical properties of a novel compatibilized recycled polyethylene terephthalate/polyamide 11 (rPET/PA11) blends. eXPRESS Polym. Lett. **15**(12), 1206–1215 (2021). https://doi.org/10.3144/EXPRESSPOLYMLETT.2021.96
10. Wang, H.X., Ramakrishnan, K.R., Shankar, K.: Experimental study of the medium velocity impact response of sandwich panels with different cores. Mater. Des. **99**, 68–82 (2016). https://doi.org/10.1016/j.matdes.2016.03.048
11. Meo, M., Vignjevic, R., Marengo, G.: The response of honeycomb sandwich panels under low-velocity impact loading. Int. J. Mech. Sci. **47**(9), 1301–1325 (2005). https://doi.org/10.1016/j.ijmecsci.2005.05.006
12. Kosedag, E., Ekici, R.: Low-velocity and ballistic impact resistances of particle reinforced metal–matrix composites: an experimental study. J. Compos. Mater. **56**(7), 991–1002 (2022). https://doi.org/10.1177/00219983211068101
13. Khan, Z.I., Mohamad, Z.B., Rahmat, A.R.B., et al.: A novel recycled polyethylene terephthalate/polyamide 11 (rPET/PA11) thermoplastic blend. Prog. Rubber Plast. Recycl. Technol. **37**(3), 233–244 (2021). https://doi.org/10.1177/14777606211001074
14. Wei, X., Li, D., Xiong, J.: Fabrication and mechanical behaviors of an all-composite sandwich structure with a hexagon honeycomb core based on the tailor-folding approach. Compos. Sci. Technol. **184**, 107878 (2019). https://doi.org/10.1016/j.compscitech.2019.107878
15. Wei, X., Wu, Q., Gao, Y., et al.: Bending characteristics of all-composite hexagon honeycomb sandwich beams: experimental tests and a three-dimensional failure mechanism map. Mech. Mater. **148**, 103401 (2020). https://doi.org/10.1016/j.mechmat.2020.103401
16. Li, J., Zhang, W., Wang, Z., et al.: Dynamic response and failure of CFRP Kagome lattice core sandwich panels subjected to low-velocity impact. Int. J. Impact Eng. **181**, 104737 (2023). https://doi.org/10.1016/j.ijimpeng.2023.104737
17. Zeng, W., Jiang, W., Liu, J., et al.: Fabrication method and dynamic responses of composite sandwich structure with reentrant honeycomb cores. Compos. Struct. **299**, 116084 (2022). https://doi.org/10.1016/j.compstruct.2022.116084

18. Yu, S., Yu, X., Ao, Y., et al.: The impact resistance of composite Y-shaped cores sandwich structure. Thin-Walled Struct. **169**, 108389 (2021). https://doi.org/10.1016/j.tws.2021.108389

19. Khaliulin, V.I., Sh, G.R., Markovtsev, V.A., et al.: Process of forming mirror-shaped relief plates of folded structure. Vestnik of Samara University. Aerosp. Mech. Eng. **18**(4), 180 (2019). https://doi.org/10.18287/2541-7533-2019-18-4-169-182

20. Sun, G., Huo, X., Chen, D., et al.: Experimental and numerical study on honeycomb sandwich panels under bending and in-panel compression. Mater. Des. **133**, 154–168 (2017). https://doi.org/10.1016/j.matdes.2017.07.057

21. Sun, G., Chen, D., Huo, X., et al.: Experimental and numerical studies on indentation and perforation characteristics of honeycomb sandwich panels. Compos. Struct. **184**, 110–124 (2018). https://doi.org/10.1016/j.compstruct.2017.09.025

22. Sun, G., Huo, X., Wang, H., et al.: On the structural parameters of honeycomb-core sandwich panels against low-velocity impact. Compos. B Eng. **216**, 108881 (2021). https://doi.org/10.1016/j.compositesb.2021.108881

23. Sun, G., Chen, D., Wang, H., et al.: High-velocity impact behaviour of aluminium honeycomb sandwich panels with different structural configurations. Int. J. Impact Eng. **122**, 119–136 (2018). https://doi.org/10.1016/j.ijimpeng.2018.08.007

24. Yang, K., Li, Z., Ge, D.: Quasi-static and dynamic out-of-plane crashworthiness of 3D curved-walled mixed-phase honeycombs. Thin-Walled Struct. **182**, 110305 (2023). https://doi.org/10.1016/j.tws.2022.110305

25. Qi, J.Q., Li, C., Tie, Y., et al.: Energy absorption characteristics of origami-inspired honeycomb sandwich structures under low-velocity impact loading. Mater. Des. **207**, 109837 (2021). https://doi.org/10.1016/j.matdes.2021.109837

26. Pehlivan, L., Baykasoğlu, C.: An experimental study on the compressive response of CFRP honeycombs with various cell configurations. Compos. B Eng. **162**, 653–661 (2019). https://doi.org/10.1016/j.compositesb.2019.01.044

27. Qiu, X.M., Zhang, J., Yu, T.X.: Collapse of periodic planar lattices under uniaxial compression, part II: dynamic crushing based on finite element simulation. Int. J. Impact Eng. **36**(10–11), 1231–1241 (2009). https://doi.org/10.1016/j.ijimpeng.2009.05.010

28. Ruan, D., Lu, G., Wang, B., et al.: In-plane dynamic crushing of honeycombs—a finite element study. Int. J. Impact Eng. **28**(2), 161–182 (2003). https://doi.org/10.1016/s0734-743x(02)00056-8

29. Wang, Y., Yu, Y., Wang, C., et al.: On the out-of-plane ballistic performances of hexagonal, reentrant, square, triangular and circular honeycomb panels. Int. J. Mech. Sci. **173**, 105402 (2020). https://doi.org/10.1016/j.ijmecsci.2019.105402

30. Ul Haq, A., Gunashekar, G., Narala, S.K.R.: The dynamic response of AuxHex and Star-Reentrant honeycomb cored sandwich panels subject to blast loading. Arab. J. Sci. Eng. (2023). https://doi.org/10.1007/s13369-022-07564-0

31. Deng, Y., Zhou, N., Li, X., et al.: Dynamic response and failure mechanism of S-shaped CFRP foldcore sandwich structure under low-velocity impact. Thin-Walled Struct. **173**, 109007 (2022). https://doi.org/10.1016/j.tws.2022.109007

32. Deng, Y., Li, X., Hu, X., et al.: Low-velocity impact behavior of interlayer hybrid foldcore sandwich structures with carbon/glass fibers. Mech. Adv. Mater. Struct. (2023). https://doi.org/10.1080/15376494.2023.2172236

33. Deng, Y.F., Hu, X.Y., Yang, X.Y., et al.: Dynamic response of Nomex honeycomb sandwich panels subjected to aluminum foam projectile impact–an experimental study. Polym. Compos. **44**(2), 1017–1037 (2023). https://doi.org/10.1002/pc.27151

34. ASTM, D7316-05. Standard test method for measuring the damage resistance of a fiber-reinforced polymer matrix composite to a drop-weight impact event. (2014)

35. He, W., Yao, L., Meng, X., et al.: Effect of structural parameters on low-velocity impact behavior of aluminum honeycomb sandwich structures with CFRP face sheets. Thin-Walled Struct. **137**, 411–432 (2019). https://doi.org/10.1016/j.tws.2019.01.022

36. Zhao, Y., Yang, Z., Yu, T., et al.: Mechanical properties and energy absorption capabilities of aluminium foam sandwich structure subjected to low-velocity impact. Constr. Build. Mater. **273**, 121996 (2021). https://doi.org/10.1016/j.conbuildmat.2020.121996

37. Tian, J., Xu, T., An, L., et al.: Study on behavior and mechanism of low-velocity impact and post-impact flexural properties of carbon-aramid/epoxy resin laminated composites. Compos. Struct. **300**, 116166 (2022). https://doi.org/10.1016/j.compstruct.2022.116166

38. Zhang, X., Xu, F., Zang, Y., et al.: Experimental and numerical investigation on damage behavior of honeycomb sandwich panel subjected to low-velocity impact. Compos. Struct. **236**, 111882 (2020). https://doi.org/10.1016/j.compstruct.2020.111882

39. Khosravani, M.R., Rezaei, S., Ruan, H., et al.: Fracture behavior of anisotropic 3D-printed parts: experiments and numerical simulations. J. Market. Res. **19**, 1260–1270 (2022). https://doi.org/10.1016/j.jmrt.2022.05.068

40. Chen, Y., Hou, S., Fu, K., et al.: Low-velocity impact response of composite sandwich structures: modelling and experiment. Compos. Struct. **168**, 322–334 (2017). https://doi.org/10.1016/j.compstruct.2017.02.064

41. Labeas, G., Johnson, A., Mines, R., et al.: The impact performance of sandwich structures with innovative cellular metal and folded composite cores[C]//SAMPE Europe Int. Conf.DLR, 2009. DOI:Labeas, George und Johnson, Alastair und Mines, Robert und Klaus

42. Xue, X., Zhang, C., Chen, W., et al.: Study on the impact resistance of honeycomb sandwich structures under low-velocity/heavy mass. Compos. Struct. **226**, 111223 (2019). https://doi.org/10.1016/j.compstruct.2019.111223

43. He, W., Liu, J., Tao, B., et al.: Experimental and numerical research on the low velocity impact behavior of hybrid corrugated core sandwich structures. Compos. Struct. **158**, 30–43 (2016). https://doi.org/10.1016/j.compstruct.2016.09.009

44. Liu, L., Meng, P., Wang, H., et al.: The flatwise compressive properties of Nomex honeycomb core with debonding imperfections in the double cell wall. Compos. B Eng. **76**, 122–132 (2015). https://doi.org/10.1016/j.compositesb.2015.02.017

45. Hu, L.L., He, X.L., Wu, G.P., et al.: Dynamic crushing of the circular-celled honeycombs under out-of-plane impact. Int. J. Impact Eng. **75**, 150–161 (2015). https://doi.org/10.1016/j.ijimpeng.2014.08.008

46. Zhu, G., Sun, G., Li, G., et al.: Modeling for CFRP structures subjected to quasi-static crushing. Compos. Struct. **184**, 41–55 (2018). https://doi.org/10.1016/j.compstruct.2017.09.001

47. Patel, S., Patel, M.: The efficient design of hybrid and metallic sandwich structures under air blast loading. J. Sandwich Struct. Mater. **24**(3), 1706–1725 (2022). https://doi.org/10.1177/10996362211065748

48. Nia, A.A., Hamedani, J.H.: Comparative analysis of energy absorption and deformations of thin walled tubes with various section geometries. Thin-Walled Struct. **48**(12), 946–954 (2010). https://doi.org/10.1016/j.tws.2010.07.003

49. Gao, W., Yu, Z., Ma, A., et al.: Numerical simulation of composite grid sandwich structure under low-velocity impact. Sci. Eng. Compos. Mater. **29**(1), 516–528 (2022). https://doi.org/10.1515/secm-2022-0176